

## ***Electronic Supplementary Information (ESI)***

Potassium mediated Co-Fe-based Prussian blue analogue architectures for aqueous potassium-ion storage

Xijun Wei,<sup>‡a</sup> Jiacheng Wei,<sup>‡b</sup> Yingze Song,<sup>\*a</sup> Donghai Wu,<sup>c</sup> Xu Dong Liu,<sup>d</sup> Houyang Chen,<sup>\*e</sup> Peng Xiao<sup>f</sup> and Yunhuai Zhang<sup>f</sup>

<sup>a</sup> State Key Laboratory of Environment-Friendly Energy Materials, School of Materials Science and Engineering, Graphene Joint Innovation Centre, Southwest University of Science and Technology, Mianyang, Sichuan, 621010, China

<sup>b</sup> Shenzhen Key Laboratory of Polymer Science and Technology, College of Materials Science and Engineering, Shenzhen University, Shenzhen, 518060, China

<sup>c</sup> Henan Key Laboratory of Nanocomposites and Applications, Institute of Nanostructured Functional Materials, Huanghe Science and Technology College, Zhengzhou, 450006, China

<sup>d</sup> Research Centre of Laser Fusion, China Academy of Engineering Physics, Mianyang, 621900, P. R. China

<sup>e</sup> Department of Chemical and Biological Engineering, State University of New York at Buffalo, Buffalo, New York, 14260-4200, USA

<sup>f</sup> College of Chemistry and Chemical Engineering, Chongqing University, Chongqing, 400044, China

<sup>‡</sup> X. Wei and J. Wei contributed equally to this article

\*Corresponding authors: yzsong@swust.edu.cn (Y. Song); hchen23@buffalo.edu (H. Chen)

## **1. Experimental Section**

### **1.1 Materials**

All the chemicals were used directly without further treatment in the experiment. Both  $\text{K}_3[\text{Co}(\text{CN})_6]$  and  $\text{K}_3[\text{Fe}(\text{CN})_6]$  were purchased from Aladdin Biological Technology.  $\text{Ni}(\text{NO}_3)_2 \cdot 6\text{H}_2\text{O}$ ,  $\text{Co}(\text{NO}_3)_2 \cdot 6\text{H}_2\text{O}$ ,  $\text{K}_2\text{SO}_4$  and  $\text{KCl}$  were purchased from Sigma-Aldrich Co., Ltd.

### **1.2 Synthesis of potassium-rich $\text{K}_2\text{Co}[\text{Fe}(\text{CN})_6]$ and potassium-poor $\text{KNi}[\text{Co}(\text{CN})_6]$**

The synthesis procedure of potassium-rich  $\text{K}_2\text{Co}[\text{Fe}(\text{CN})_6]$  is depicted as follows: typically, 2 mmol of  $\text{K}_3[\text{Fe}(\text{CN})_6]$  and 0.16 mol of  $\text{KCl}$  were dissolved in 150 mL deionized water under stirring for 10 min (Solution A). 5 mmol of  $\text{Co}(\text{NO}_3)_2 \cdot 6\text{H}_2\text{O}$  was dissolved in 150 mL deionized water under stirring for 10 min (Solution B). Then, the solution A and B were mixed under magnetic stirring. The mixture was placed at room temperature for 24 hours. Finally, the obtained purple products were filtered and washed several times with deionized water and absolute ethanol and finally dried in a vacuum oven at 60 °C overnight. The potassium-poor  $\text{KNi}[\text{Co}(\text{CN})_6]$  was gained throughout the similar synthesis procedure by using  $\text{K}_3[\text{Co}(\text{CN})_6]$ ,  $\text{KCl}$  and  $\text{Ni}(\text{NO}_3)_2 \cdot 6\text{H}_2\text{O}$ .

## **2. Material characterization**

Scanning electron microscopy (SEM) images were acquired on a JEOL JSM 7800F microscope operated at 5 kV. Transmission electron microscopy (TEM) images were taken on JEOL 2100F microscopes. X-ray diffraction (XRD) patterns

were collected on a Bruker D8 Advanced X-Ray Diffractometer with Ni filtered Cu  $K\alpha$  radiation ( $\lambda=1.5406 \text{ \AA}$ ) at a voltage of 40 kV and a current of 40 mA. FTIR transmittance spectra were recorded using a 60-SXB IR spectrometer. Nitrogen adsorption-desorption isotherm were obtained by using an AUTOSPRB-1 (Quantachrome Instruments)  $N_2$  adsorption apparatus at temperature of liquid  $N_2$ . XPS analysis was conducted on a VG ESCALAB MKII spectrometer using an  $MgK\alpha$  X-ray source (1253.6 eV, 120 W) at a constant analyzer.

### **3. Electrochemical measurements**

To evaluate the electrochemical performance of the as-prepared  $K_2Co[Fe(CN)_6]$  and  $KNi[Co(CN)_6]$ , the working electrode were prepared by dispersing the as-obtained products (80 wt%), conductive carbon black (10 wt%, Super-P-Li) and polytetrafluoroethylene (10 wt%, PTFE) in ethyl alcohol. The mixture was then pressed onto a Ni foam and dried at 60 °C for 12 h under vacuum. The mass loading of the active material was around 3.0 mg  $cm^{-2}$ . Electrochemical measurements were conducted in an aqueous  $K_2SO_4$  electrolyte (0.5 M) using a three-electrode system, where a Hg/HgO electrode served as the reference electrode and a Pt foil acted as the counter electrode. Both the galvanostatic charge-discharge (GCD), cyclic voltammetry (CV) and electrochemical impedance spectra (EIS) studies were carried out on a CHI 660E electrochemical workstation. The cycling stability was performed on a LAND battery system. To investigate structural and phase changes, the active material was charged and discharged to different states, washed with distilled water and examined by using ex-situ XRD tests.

#### **4. Computational details**

The spin-polarized DFT calculations were carried out with the first-principles method and implemented by Vienna ab initio simulation package (VASP).<sup>[1]</sup> The exchange-correlations were treated by the generalized gradient approach (GGA) with the Perdew-Burke-Ernzerhof (PBE) functional.<sup>[2]</sup> Because of the drawback in describing the strong exchange-correlation effect of 3d orbitals, the additional Hubbard parameter correction was adopted, with the U–J of 3.2 eV and 4.3 eV for Co and Fe atoms,<sup>[3, 4]</sup> respectively. The energy cutoff of the wave function was set to 500 eV. Brillouin zones were sampled by a Monkhorst–Pack k-point mesh with a  $3 \times 3 \times 3$  k-point grid.<sup>[5]</sup> All atoms were allowed to be fully relaxed until the convergence tolerance of energy and maximum force were smaller than  $10^{-6}$  eV/atom and 0.05 eV/Å, respectively. The climbing-image nudged elastic band (CI-NEB) method was used to explore the diffusion behavior of potassium-ion.<sup>[6]</sup>

*Supplementary Information Figures*

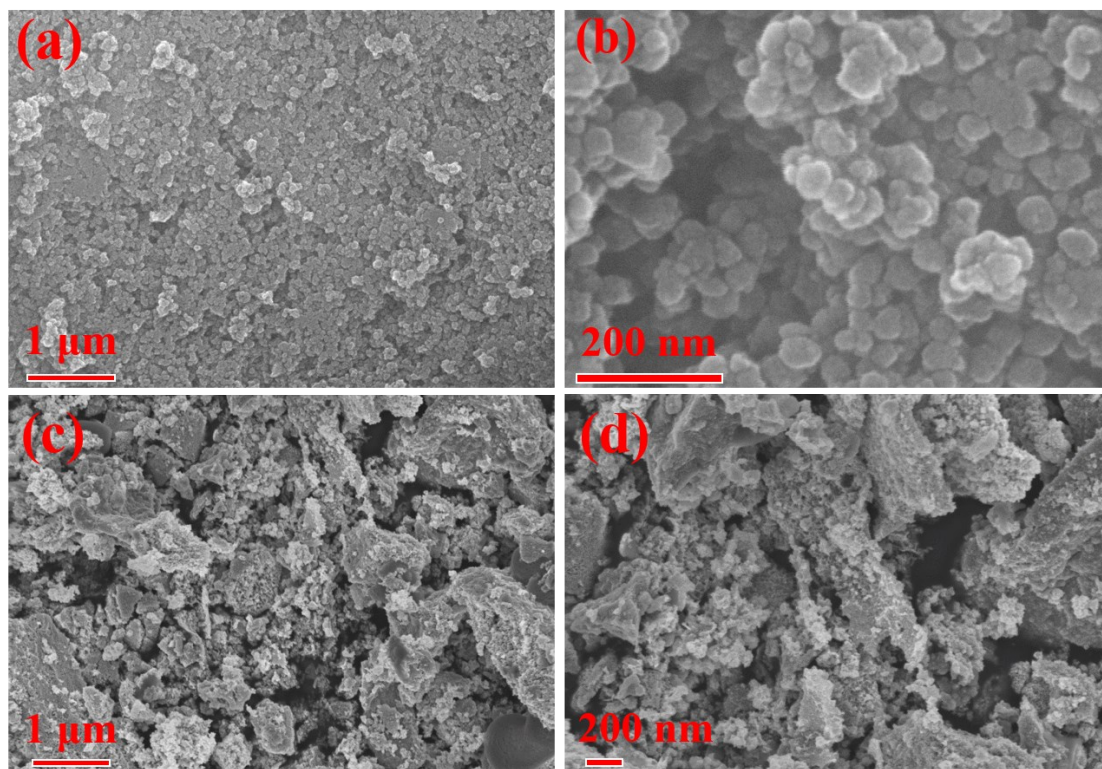


**Figure S1.** SEM images of the as-prepared (a, b)  $K_2Co[Fe(CN)_6]$  and (c, d)  $KNi[Co(CN)_6]$ .

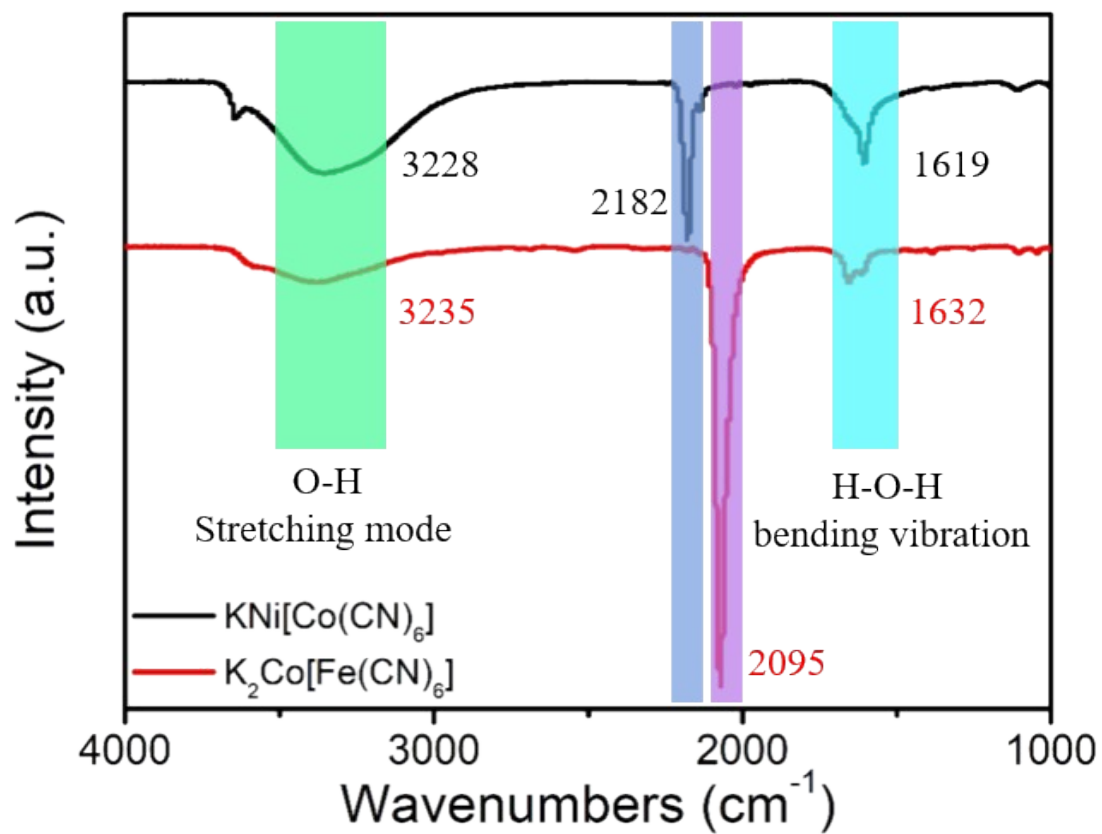


**Figure S2.** FTIR spectra of  $\text{K}_2\text{Co}[\text{Fe}(\text{CN})_6]$  and  $\text{KNi}[\text{Co}(\text{CN})_6]$ .

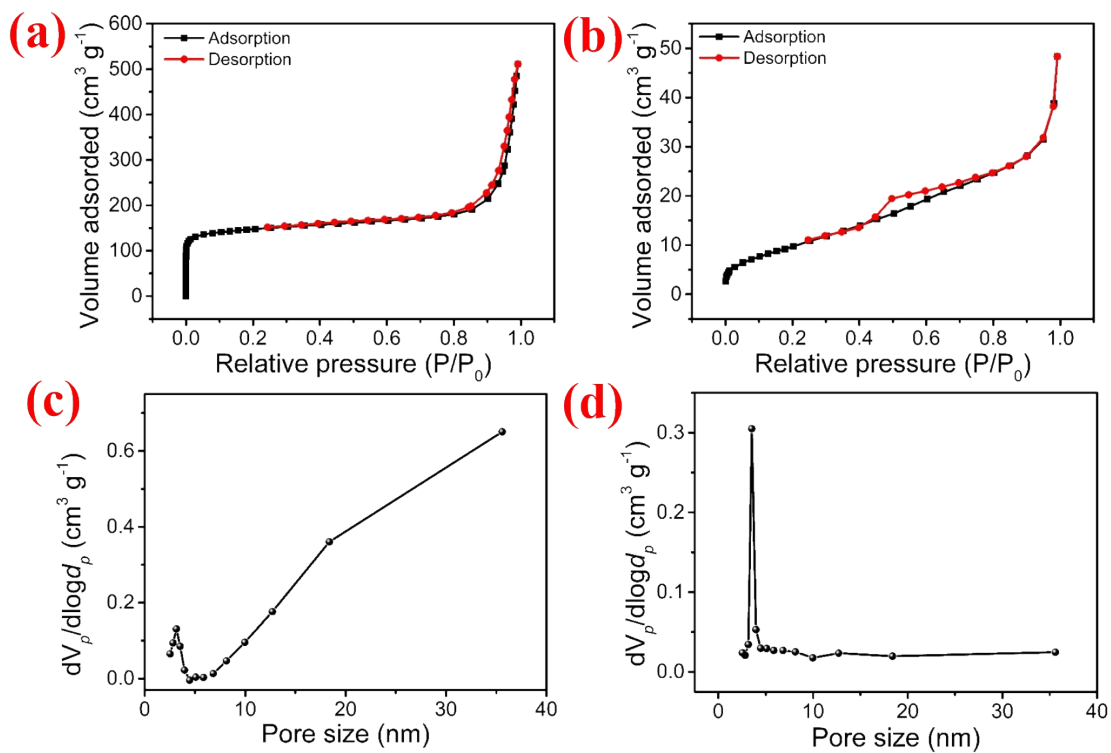


**Figure S3.** (a, b) Nitrogen adsorption-desorption isotherms of  $K_2Co[Fe(CN)_6]$  and  $KNi[Co(CN)_6]$ . (c, d) BJH pore size distribution curves of  $K_2Co[Fe(CN)_6]$  and  $KNi[Co(CN)_6]$ .

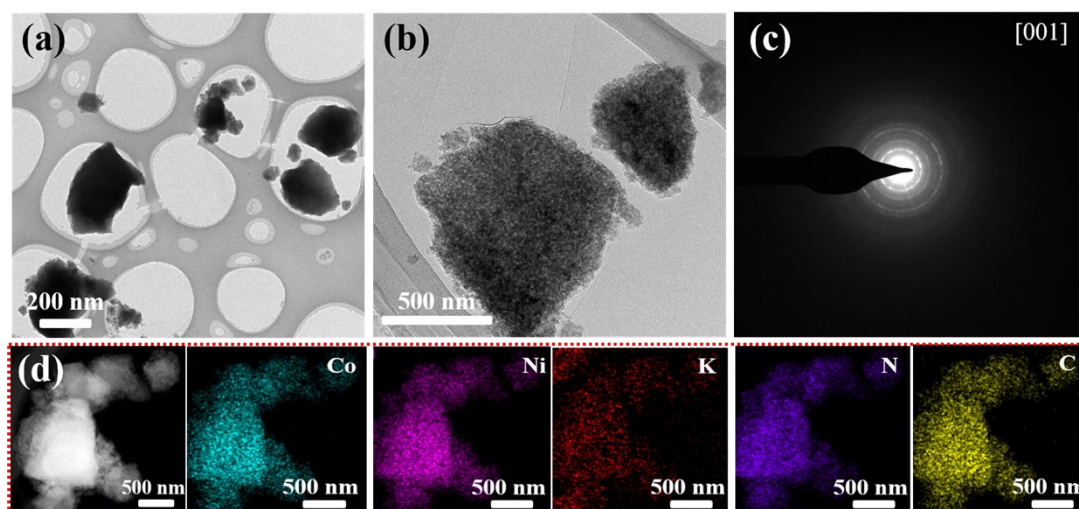


**Figure S4.** (a, b) The TEM images of  $\text{KNi}[\text{Co}(\text{CN})_6]$  with different magnification. (c) The corresponding SAED pattern from Figure S3b. (d) The HAADF-STEM and element mapping of  $\text{KNi}[\text{Co}(\text{CN})_6]$ .

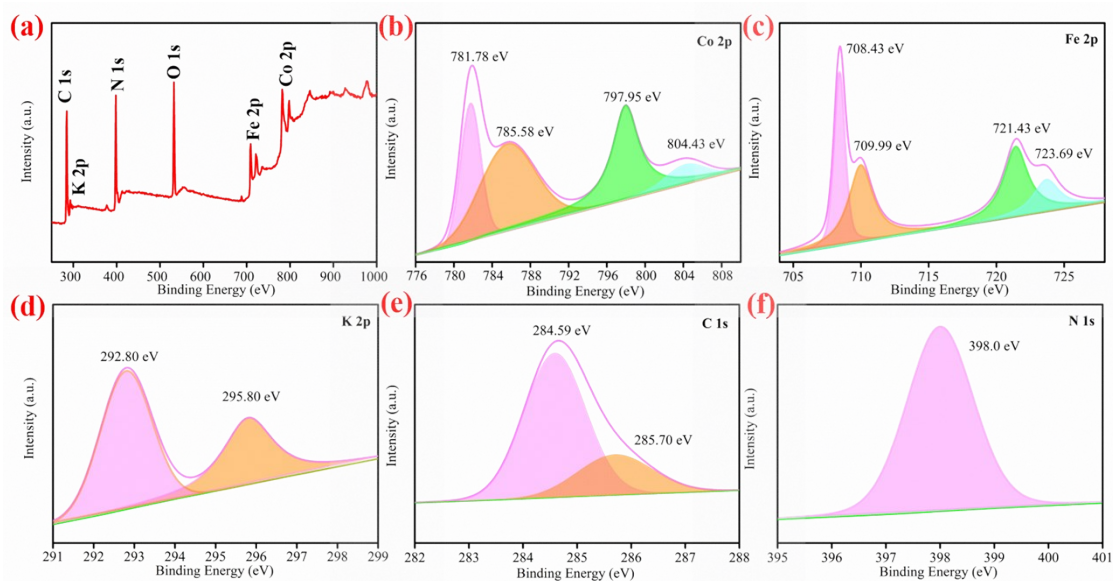


**Figure S5.** (a) The full XPS survey of the  $\text{K}_2\text{Co}[\text{Fe}(\text{CN})_6]$ . The high-resolution spectra of (b) Co 2p, (c) Fe 2p, (d) K 2p, (e) C 1s and (f) N 1s, respectively.

The XPS measurement was used to confirm the valence states of the as-prepared samples. The survey spectrum of  $\text{K}_2\text{Co}[\text{Fe}(\text{CN})_6]$  in Figure S5a illustrates the co-existence of Co, Fe, K, C, N and O elements, where O element is assigned to the presence of water in final products. Figure S5b shows the high-resolution spectrum of Co 2p, where the peaks located at 781.78 and 797.95 eV are assigned to Co  $2p_{3/2}$  and Co  $2p_{1/2}$ , while the peaks located at 785.58 and 804.43 eV are corresponding satellites, respectively, indicating the existence of  $\text{Co}^{2+}$  and  $\text{Co}^{3+}$  in  $\text{K}_2\text{Co}[\text{Fe}(\text{CN})_6]$ .<sup>[7]</sup> The peaks located at 708.43 and 709.99 eV are assigned to Fe  $2p_{3/2}$ , and the peaks located at 721.43 and 723.69 eV are assigned to Fe  $2p_{1/2}$  (Figure S5c), which confirms the presence of  $\text{Fe}^{2+}$  and  $\text{Fe}^{3+}$ .<sup>[7, 8]</sup> In addition, the peaks located at 292.80 and 295.80 eV can be assigned to K  $2p_{3/2}$  and K  $2p_{1/2}$  (Figure S5d), demonstrated the existence of  $\text{K}^+$ . Moreover, the high-resolution spectrum of C 1s is shown in Figure S5e, in accordance with the results of element maps. The N 1s peak centering at 398.0 eV corresponding to the nitrogen in the cyano-ligan (Figure S5f).<sup>[9]</sup>

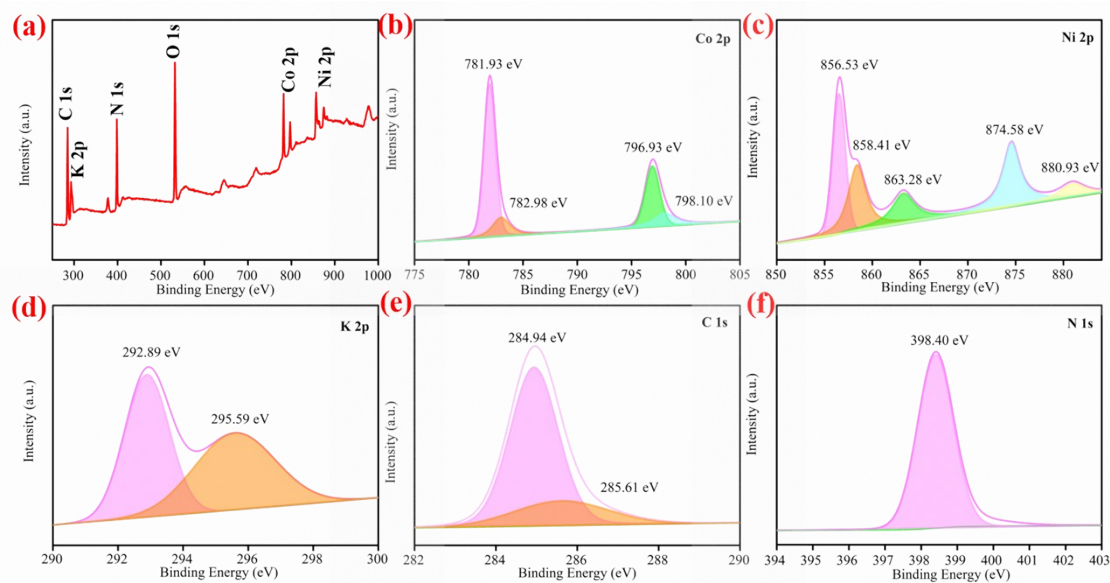


**Figure S6.** (a) The full XPS survey of the  $\text{KNi}[\text{Co}(\text{CN})_6]$ . The high-resolution spectra of (b) Co 2p, (c) Ni 2p, (d) K 2p, (e) C 1s and (f) N 1s, respectively.

The survey spectrum of  $\text{KNi}[\text{Co}(\text{CN})_6]$  indicates the principal elements of Co, Ni, K, C, N and O (Figure S6a). As seen in the high-resolution spectrum of Co 2p, the peaks at 781.93 and 782.98 eV are indexed to Co  $2p_{3/2}$ , and the peaks located at 796.93 and 798.10 eV are assigned to Co  $2p_{1/2}$ , disclosing the coexistence of  $\text{Co}^{2+}$  and  $\text{Co}^{3+}$  in  $\text{KNi}[\text{Co}(\text{CN})_6]$  (Figure S6b).<sup>[7, 10]</sup> The peaks centered at 856.53 and 858.41 eV belong to Ni  $2p_{3/2}$ , and the peak located at 874.58 is assigned to Ni  $2p_{1/2}$  with a satellite at 880.93 eV (Figure S6c), demonstrating the signal of  $\text{Ni}^{2+}$ .<sup>[9, 11]</sup> Additionally, the peaks at 292.80 and 295.80 eV are indexed to K  $2p_{3/2}$  and K  $2p_{1/2}$  (Figure S6d), verifying the existence of  $\text{K}^+$ . Furthermore, the high-resolution spectra of C 1s is exhibited in Figure S6e. The N 1 s peak at 398.4 eV can also be assigned to the nitrogen in cyano-ligan (Figure S6f).<sup>[9]</sup>

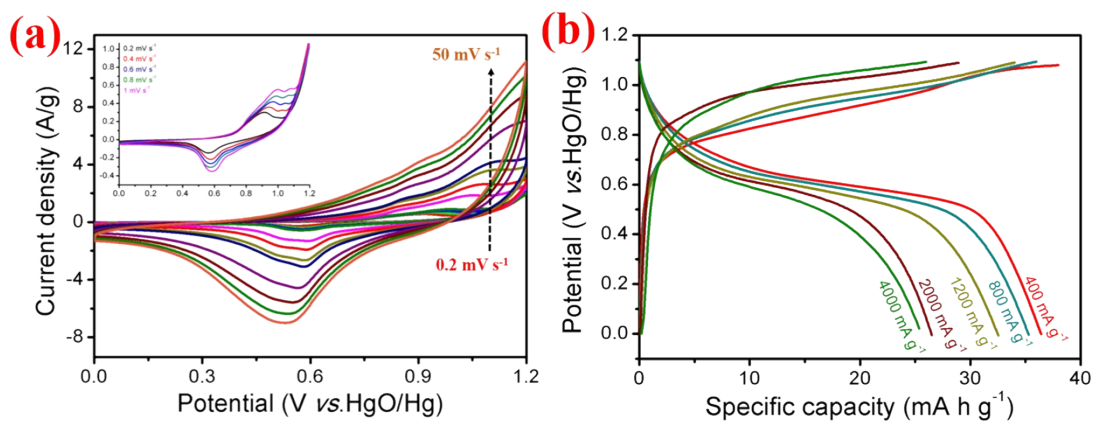


**Figure S7.** (a) the CV curves of KNi[Co(CN)<sub>6</sub>] at various scan rates from 0.2–50 mV s<sup>-1</sup>. (b) The GCD curves of KNi[Co(CN)<sub>6</sub>] at various current densities from 400–4000 mA g<sup>-1</sup>.

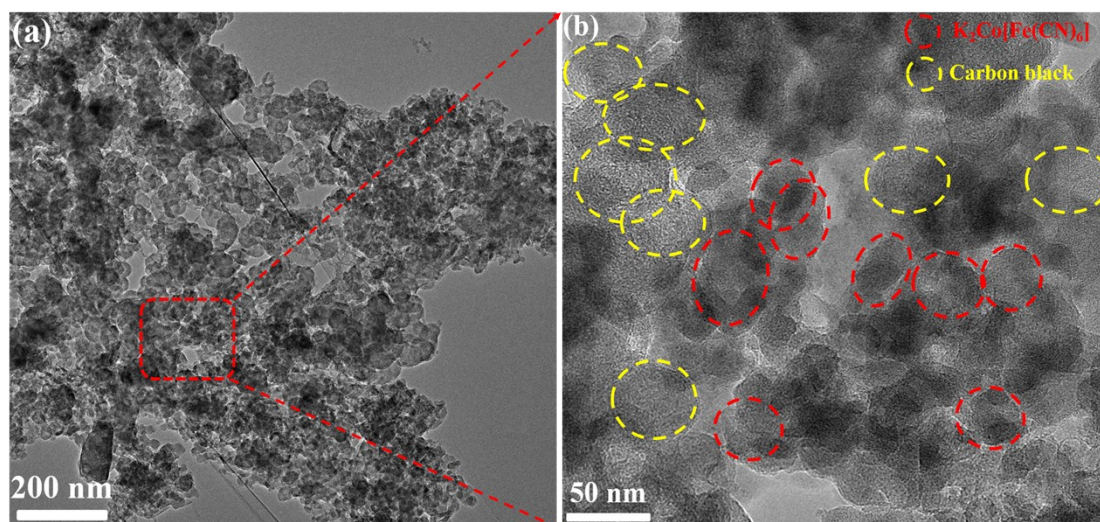


**Figure S8.** (a), (b) The TEM and HRTEM images of  $\text{K}_2\text{Co}[\text{Fe}(\text{CN})_6]$  after 1000 cycles at  $4000 \text{ mA g}^{-1}$ .

As shown in Figure S8, the particle size of  $\text{K}_2\text{Co}[\text{Fe}(\text{CN})_6]$  is around 40–50 nm after 1000 cycles at  $4000 \text{ mA g}^{-1}$ , manifesting a slight change after cycling test (as shown in Figure 3a and 3b).

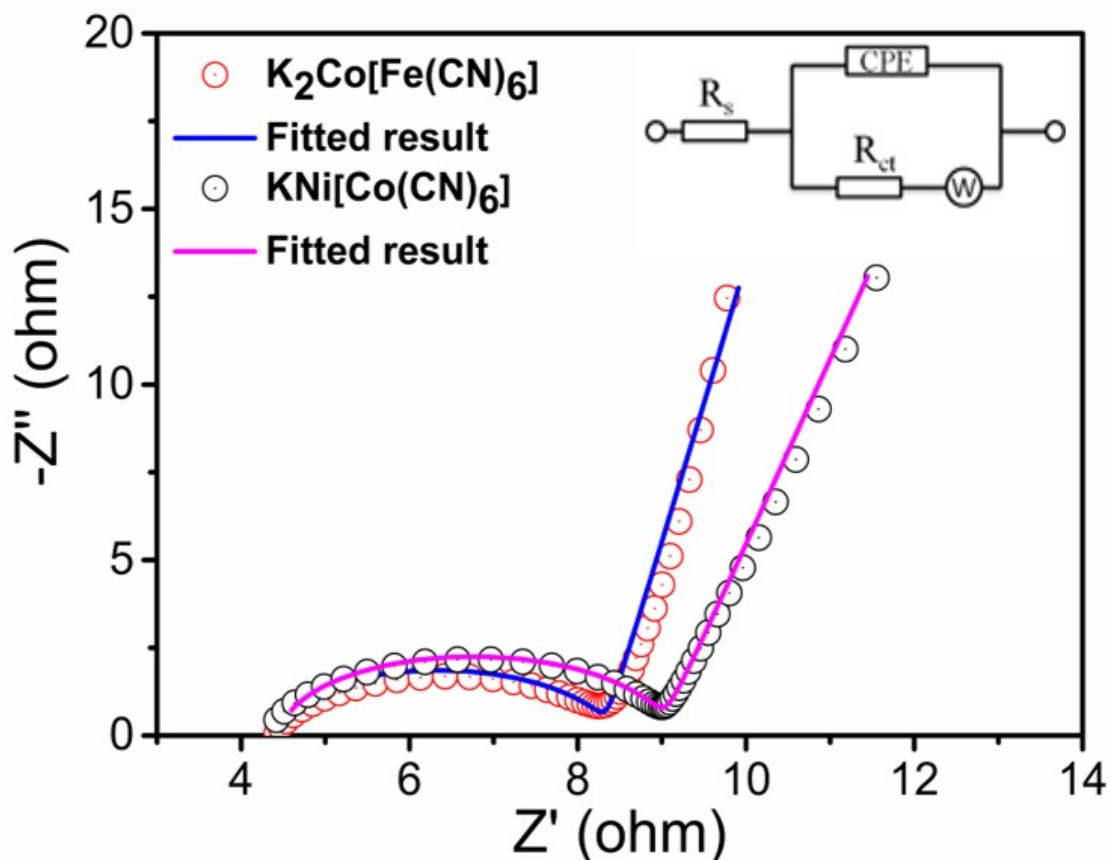


**Figure S9.** Nyquist plots of the  $K_2Co[Fe(CN)_6]$  and  $KNi[Co(CN)_6]$  and the inset exhibits the corresponding equivalent circuits.

The EIS tests of  $K_2Co[Fe(CN)_6]$  and  $KNi[Co(CN)_6]$  were recorded with the frequency range from 100 kHz to 0.01 Hz. The Nyquist plots with three parts are illustrated in Figure S9. Typically, the intercept on the real axis is the sum of ionic resistances of the electrolyte ( $R_s$ ), and the diameter of the semi-circle in the high-frequency region represents the charge-transfer resistance ( $R_{ct}$ ) at the current collector-electrode materials and electrode materials-electrolyte interface. Additionally, a straight line in the low-frequency region indicates the ion diffusion resistance. The  $R_{ct}$  values of  $K_2Co[Fe(CN)_6]$  and  $KNi[Co(CN)_6]$  are 4.05  $\Omega$  and 4.79  $\Omega$ , respectively, indicating the better conductivity of  $K_2Co[Fe(CN)_6]$  than  $KNi[Co(CN)_6]$ .

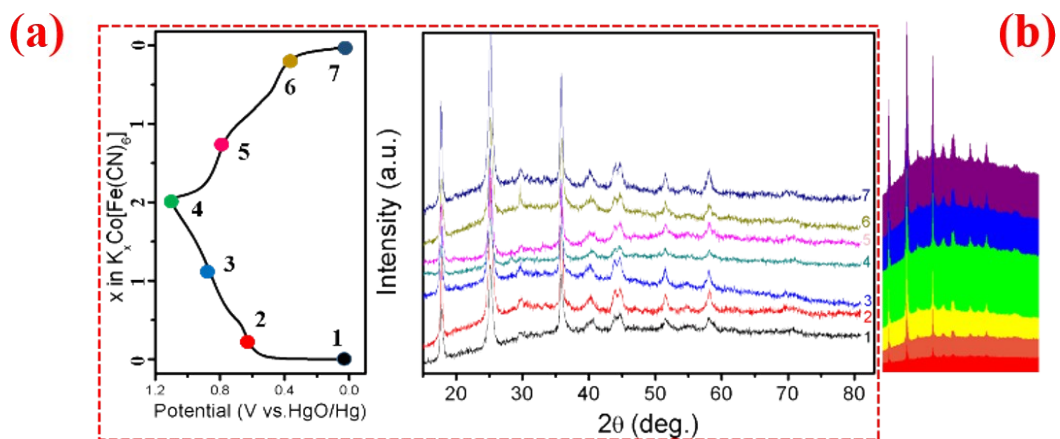


**Figure S10.** (a) Ex-situ XRD patterns of  $\text{K}_2\text{Co[Fe(CN)}_6]$  architectures at different charge/discharge states as marked in the galvanostatic charge/discharge curve. (b) The color graphic from ex-situ XRD patterns.

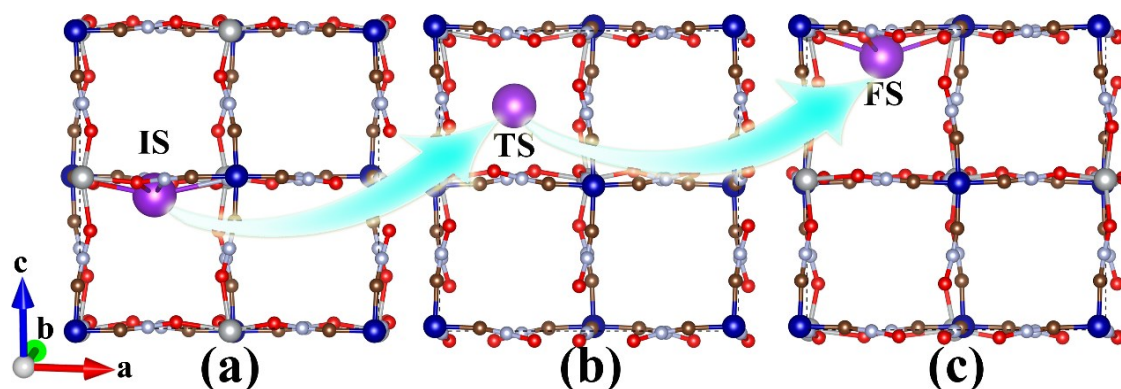


**Figure S11.** The initial state (a), transition state (b), and the final state (c) of a potassium-ion diffusion within the lattice of the  $\text{K}_2\text{Co}[\text{Fe}(\text{CN})_6]$  model structure. The purple, blue, khaki, red, silver, and brown ball represents the K, Co, Fe, O, N, and C atoms, respectively.

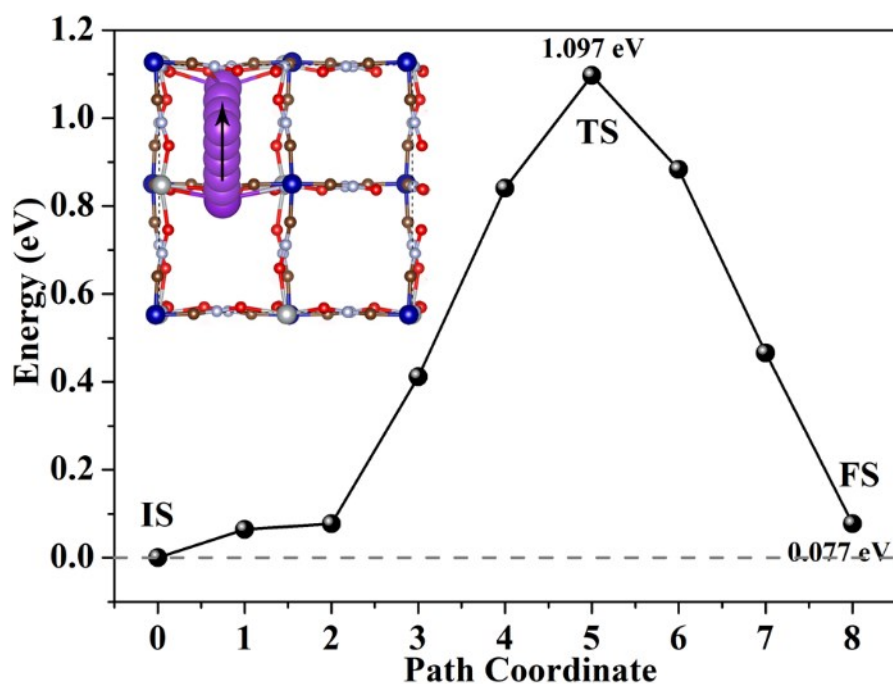


**Figure S12.** Migration energy barriers of a potassium-ion diffusion within the lattice of the  $\text{K}_2\text{Co}[\text{Fe}(\text{CN})_6]$  model structure. The inset shows the calculated  $\text{K}^+$  migration paths.

To understand the diffusion behaviors of a  $\text{K}^+$ -ion, a migration path along the [001] direction within the lattice of the  $\text{K}_2\text{Co}[\text{Fe}(\text{CN})_6]$  was studied. The corresponding initial state, transition state, and the final state are shown in Figure S11. The calculated migration energy barrier is 1.097 eV (Figure S12), which is much smaller than that of  $\text{K}^+$ -ion diffusion within the lattice of  $\text{K}_2\text{Fe}^{\text{II}}[\text{Fe}^{\text{II}}(\text{CN})_6]$  (1.66 eV) and  $\text{K}_2\text{Ni}[\text{Fe}^{\text{II}}(\text{CN})_6]$  (1.85 eV).<sup>[12]</sup>

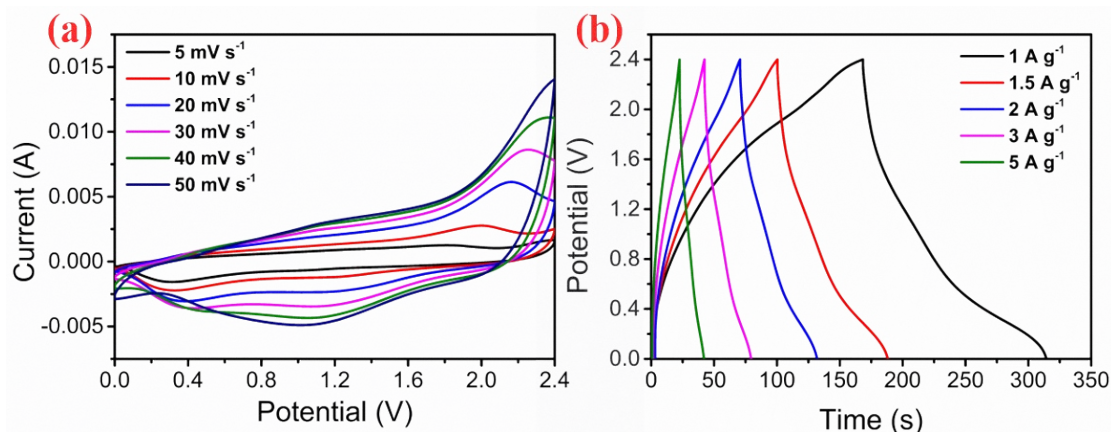


**Figure S13.** (a) CV curves of AC//K<sub>2</sub>Co[Fe(CN)<sub>6</sub>] at various scan rates from 5 to 50 mV s<sup>-1</sup>; (b) GCD curves of AC//K<sub>2</sub>Co[Fe(CN)<sub>6</sub>] at different current densities from 1 to 5 A g<sup>-1</sup>.

To evaluate the practical application potential of the as-prepared K<sub>2</sub>Co[Fe(CN)<sub>6</sub>], a two-electrode device was assembled. The commercial activated carbon (AC) was directly used as the negative electrode and the as-prepared K<sub>2</sub>Co[Fe(CN)<sub>6</sub>] was employed as the positive electrode (AC//K<sub>2</sub>Co[Fe(CN)<sub>6</sub>]). Figure S13a shows the CV curves of AC//K<sub>2</sub>Co[Fe(CN)<sub>6</sub>] at scan rates of 10–50 mV s<sup>-1</sup>, which shows redox peaks caused by the intercalation/deintercalation of K<sup>+</sup>-ions. The shape of CV curves is kept well with the increase of scan rate, demonstrating its superior reversibility and fast charge-discharge process. The energy storage performance was further detected by GCD measurements at various current densities (Figure S13b). According to the discharge time, the energy density of AC//K<sub>2</sub>Co[Fe(CN)<sub>6</sub>] device is 46.67 Wh kg<sup>-1</sup> at a power density of 1200 W kg<sup>-1</sup>, and even at a high power density of 6000 W kg<sup>-1</sup>, the device still exhibits an energy density of 33.33 Wh kg<sup>-1</sup>, substantiating its simultaneous high energy density and power density.

**Table S1** Performance comparison of as-prepared  $\text{K}_2\text{Co}[\text{Fe}(\text{CN})_6]$  with that of other reported materials in aqueous potassium ions storage realm.

Materials	Electrolyte	Capacity ( $\text{mA h g}^{-1}$ )	Current density ( $\text{mA g}^{-1}$ )	Ref.
$\text{K}_2\text{Fe}^{\text{II}}[\text{Fe}^{\text{II}}(\text{CN})_6] \cdot 2\text{H}_2\text{O}$	0.5 M $\text{K}_2\text{SO}_4$	120	200	[12]
$\text{K}_2\text{Ni}^{\text{II}}[\text{Fe}^{\text{II}}(\text{CN})_6] \cdot 2\text{H}_2\text{O}$	0.5 M $\text{K}_2\text{SO}_4$	42	500	
$\text{K}_2\text{NiFe}(\text{CN})_6 \cdot 1.2\text{H}_2\text{O}$	1 M $\text{KNO}_3 + 0.01$ M $\text{HNO}_3$	77.4	400	[13]
$\text{K}_{0.6}\text{Ni}_{1.2}\text{Fe}(\text{CN})_6 \cdot 3.6\text{H}_2\text{O}$	1 M $\text{KNO}_3$	59	49.8	[14]
$\text{K}_{0.71}\text{Cu}[\text{Fe}(\text{CN})_6]_{0.72} \cdot 3.7\text{H}_2\text{O}$	1 M $\text{KNO}_3 + 0.01$ M $\text{HNO}_3$	60	49.8	[15]
$\text{KCu}_{0.77}\text{Ni}_{0.23}\text{Fe}^{\text{III}}(\text{CN})_6$	1 M $\text{KNO}_3$	65	50	[16]
$\text{K}_{1.85}\text{Fe}_{0.33}\text{Mn}_{0.67}[\text{Fe}(\text{CN})_6]_{0.98} \cdot 0.7\text{H}_2\text{O}$	22 M $\text{KCF}_3\text{SO}_3$ water in salt electrolyte	130	1300	[17]
$\text{K}_2\text{Co}[\text{Fe}(\text{CN})_6]$	0.5 M	112	400	<b>This work</b>
$\text{KNi}[\text{Co}(\text{CN})_6]$	$\text{K}_2\text{SO}_4$	37	400	

## References

- [1] G. Kresse, J. Furthmüller, Efficient Iterative Schemes for Ab-Initio Total-Energy Calculations Using a Plane-Wave Basis Set, *Phys. Rev. B* 54 (1996) 11169.
- [2] J.P. Perdew, K. Burke, M. Ernzerhof, Generalized Gradient Approximation Made Simple, *Phys. Rev. Lett.* 77(18) (1996) 3865-3868.
- [3] L. Jiang, Y. Lu, C. Zhao, L. Liu, J. Zhang, Q. Zhang, X. Shen, J. Zhao, X. Yu, H. Li, X. Huang, L. Chen, Y.-S. Hu, Building aqueous K-ion batteries for energy storage, *Nat. Energy* 4(6) (2019) 495-503.
- [4] Z. Zhang, X. Zhao, S. Xi, L. Zhang, Z. Chen, Z. Zeng, M. Huang, H. Yang, B. Liu, S.J. Pennycook, P. Chen, Atomically Dispersed Cobalt Trifunctional Electrocatalysts with Tailored Coordination Environment for Flexible Rechargeable Zn–Air Battery and Self-Driven Water Splitting, *Adv. Energy Mater.* 10(48) (2020) 2002896.
- [5] H.J. Monkhorst, J.D. Pack, Special points for Brillouin-zone integrations, *Phys. Rev. B* 13(12) (1976) 5188-5192.
- [6] G. Henkelman, B.P. Uberuaga, H. Jónsson, A climbing image nudged elastic band method for finding saddle points and minimum energy paths, *J. Chem. Phys.* 113(22) (2000) 9901-9904.
- [7] L.T. Ma, S.M. Chen, C.B. Long, X.L. Li, Y.W. Zhao, Z.X. Liu, Z.D. Huang, B.B. Dong, J.A. Zapien, C.Y. Zhi, Achieving High-Voltage and High-Capacity Aqueous Rechargeable Zinc Ion Battery by Incorporating Two-Species Redox Reaction, *Adv. Energy Mater.* 9(45) (2019) 1902446.
- [8] K.J. Zhu, Z.P. Li, T. Jin, L.F. Jiao, Low defects potassium cobalt hexacyanoferrate as a superior cathode for aqueous potassium ion batteries, *J. Mater. Chem. A* 8(40) (2020) 21103-21109.
- [9] S.J. Yoon, H.T. Bui, S.J. Lee, S.A. Patil, C. Bathula, N.K. Shrestha, H. Im, Self-supported anodic film of Fe(III) redox center doped Ni-Co Prussian blue analogue frameworks with enhanced catalytic activity towards overall water electrolysis, *Journal of Electroanalytical Chemistry* 878 (2020) 114594.
- [10] W. Ahn, M.G. Park, D.U. Lee, M.H. Seo, G.P. Jiang, Z.P. Cano, F.M. Hassan, Z.W. Chen, Hollow Multivoid Nanocuboids Derived from Ternary Ni–Co–Fe Prussian Blue Analog for Dual-Electrocatalysis of Oxygen and Hydrogen Evolution Reactions, *Adv. Funct. Mater.* 28 (2018) 1802129.
- [11] M. Khalid, A. Hassan, A.M.B. Honorato, F.N. Crespilho, H. Varela, *Chem. Commun.* 54 (2018) 11048.
- [12] D.W. Su, A.M. Donagh, S.Z. Qiao, G.X. Wang, High-Capacity Aqueous Potassium-Ion Batteries for Large-Scale Energy Storage, *Adv. Mater.* 29 (2017) 1604007.
- [13] W.H. Ren, X.J. Chen, C. Zhao, Ultrafast Aqueous Potassium-Ion Batteries Cathode for Stable Intermittent Grid-Scale Energy Storage, *Adv. Energy Mater.* 8 (2018) 1801413.
- [14] C.D. Wessells, S.V. Peddada, R.A. Huggins, Y. Cui, Nickel Hexacyanoferrate Nanoparticle Electrodes for Aqueous Sodium and Potassium Ion Batteries, *Nano Lett.* 11 (2011) 5421–5425.

- [15] C.D. Wessells, R.A. Huggins, Y. Cui, Copper hexacyanoferrate battery electrodes with long cycle life and high power, *Nat. Commun.* 2(550) (2011).
- [16] C.D. Wessells, M.T. McDowell, S.V. Peddada, M. Pasta, R.A. Huggins, Y. Cui, Tunable Reaction Potentials in Open Framework Nanoparticle Battery Electrodes for Grid-Scale Energy Storage, *ACS Nano* 6(2) (2012) 1688-1694.
- [17] L.W. Jiang, Y.X. Lu, C.L. Zhao, L.L. Liu, J.N. Zhang, Q.Q. Zhang, X. Shen, J.M. Zhao, X.Q. Yu, H. Li, X.J. Huang, L.Q. Chen, Y.S. Hu, Building aqueous K-ion batteries for energy storage, *Nat. Energy* 4 (2019) 495-503.